Environmental Science Advances

ROYAL SOCIETY OF CHEMISTRY

PAPER

View Article Online
View Journal

Cite this: DOI: 10.1039/d6va00032k

Construction of novel $Mn_{0.5}Cd_{0.5}S$/BiOCl S-scheme heterojunction for ciprofloxacin degradation: mechanism and mineralization

Tunde Lewis Yusuf, *[ab] Benjamin O. Orimolade [a] and Foluso Oyedotun Agunbiade *[b]

The persistence of fluoroquinolone antibiotics such as ciprofloxacin (CIP) in aquatic environments poses serious environmental and public health risks due to their recalcitrance to conventional wastewater treatment processes. In this work, a novel $Mn_{0.5}Cd_{0.5}S$/BiOCl (MCS/BiOCl) core–shell S-scheme heterojunction photocatalyst was rationally constructed for efficient visible-light-driven degradation and mineralisation of CIP. $Mn_{0.5}Cd_{0.5}S$ nanoparticles were synthesised *via* a facile hydrothermal route and subsequently anchored onto layered BiOCl nanosheets using a green, solvent-free mechanochemical method, ensuring intimate interfacial contact and abundant heterojunction interfaces. Comprehensive structural, morphological, and surface analyses confirmed the successful formation of the heterostructure, while optical and electrochemical studies revealed enhanced visible-light absorption, suppressed charge recombination, reduced charge-transfer resistance, and an S-scheme band alignment. Under visible-light irradiation, the MCS/BiOCl composite exhibited markedly improved photocatalytic performance toward CIP degradation (92.3% removal) with a pseudo-first-order rate constant of 0.0221 min^{-1}, outperforming the individual components. Total organic carbon analysis demonstrated significant mineralisation, and photogenerated holes, superoxide radicals, and hydroxyl radicals were confirmed as the dominant reactive species, consistent with the proposed S-scheme charge-transfer mechanism. Furthermore, the composite showed promising performance in real wastewater matrices, highlighting its robustness. This study demonstrates that integrating Mn–CdS alloy nanoparticles with layered bismuth oxyhalides *via* a scalable, solvent-free approach is an effective method for designing high-performance photocatalysts for the remediation of pharmaceutical pollutants.

Received 16th January 2026
Accepted 22nd June 2026

DOI: 10.1039/d6va00032k

rsc.li/esadvances

Environmental significance

The widespread use of fluoroquinolone antibiotics, such as ciprofloxacin, in aquatic systems poses a significant environmental and public health threat, contributing to the spread of antimicrobial resistance and ecological imbalance. Conventional treatment technologies are often ineffective, transferring pollutants to secondary waste streams rather than mineralising them. In this study, we designed a stable $Mn_{0.5}Cd_{0.5}S$/BiOCl S-scheme heterojunction photocatalyst that harnesses visible light to efficiently degrade ciprofloxacin into harmless end products. The catalyst not only achieved rapid degradation but also demonstrated excellent recyclability, underscoring its potential for sustainable water purification. By combining effective light harvesting, enhanced charge separation, and a high redox potential, this work offers a practical, environmentally benign strategy for mitigating pharmaceutical pollution in water systems.

1 Introduction

The occurrence of pharmaceutical residues in aquatic environments has become a growing concern for both environmental and public health in recent years.[1,2] Among these contaminants, fluoroquinolone antibiotics such as ciprofloxacin (CIP) are frequently detected in surface water, wastewater effluents, and even drinking water sources due to their extensive consumption, incomplete metabolism in humans and livestock, and strong resistance to conventional wastewater treatment processes.[3–5] The persistence of CIP in aquatic systems can disrupt microbial communities and, more critically, contribute to the development and proliferation of antimicrobial-resistant bacteria, which poses serious ecological, societal, and economic risks.[6–8] Consequently, there is a growing demand for advanced water-treatment technologies capable of effectively degrading such recalcitrant pharmaceuticals into environmentally benign end-products under energy-efficient and cost-effective conditions.

[a]Department of Chemistry, Faculty of Natural and Agricultural Sciences, University of Pretoria, Private Bag X20, Hatfield 0028, Pretoria, South Africa. E-mail: yusuf.tl@up.ac.za

[b]Department of Chemistry, Faculty of Physical and Earth Sciences, University of Lagos, Akoka-Yaba, Lagos, Nigeria. E-mail: fagunbiade@unilag.edu.ng

Semiconductor-based photocatalysis has emerged as a promising advanced oxidation process for removing persistent organic pollutants due to its ability to generate highly reactive oxygen species (ROS) under light irradiation.[9,10] Among various photocatalytic materials, bismuth oxyhalides have attracted considerable attention, with bismuth oxychloride (BiOCl) standing out due to its layered matlockite crystal structure, intrinsic internal electric field along the {001} facets, good chemical stability, and low toxicity.[11,12] These features are favourable for charge separation and surface redox reactions. However, pristine BiOCl is characterised by a relatively wide band gap, limited visible-light absorption, and rapid recombination of photogenerated electron–hole pairs, which severely restricts its photocatalytic performance under solar or indoor-light irradiation.[13,14] To address these inherent drawbacks, several modification strategies have been explored, including defect engineering, facet control, cocatalyst loading, and the construction of heterojunctions with other semiconductors to enhance light harvesting and charge separation efficiency.

Cadmium sulfide (CdS) is a typical visible-light-responsive semiconductor with a suitable band gap for solar-energy utilisation and a conduction-band position sufficiently negative to activate molecular oxygen.[15] Despite these advantages, the practical application of CdS is hindered by serious photocorrosion and fast charge recombination.[16] Recently, alloy engineering through cation substitution has been demonstrated as an effective approach to regulate the electronic structure, improve photostability, and optimise charge dynamics of sulfide semiconductors.[17] In particular, the formation of Mn–CdS solid solutions can tailor band structures, introduce favourable defect states, and suppress photocorrosion by modifying surface reaction pathways.[18,19] When such sulfide phases are intimately coupled with layered photocatalysts such as BiOCl, a synergistic system can be achieved that combines strong visible-light absorption with efficient spatial charge separation and abundant interfacial active sites.

Beyond conventional type-II heterojunctions, S-scheme (step-scheme) heterojunctions have recently gained attention as an advanced photocatalytic architecture due to their ability to retain charge carriers with strong redox potentials. In an S-scheme system, the photogenerated electrons and holes with weaker redox ability recombine across the interface, while the electrons with higher reduction potential and holes with stronger oxidation ability are preserved in their respective semiconductors.[20–23] For a sulfide/BiOCl system, this configuration enables the accumulation of highly reducing electrons on the sulfide component and strongly oxidising holes on BiOCl, thereby facilitating the generation of reactive species such as superoxide ($^{\bullet}O_2^-$) and hydroxyl radicals ($^{\bullet}OH$).[24,25] The realisation of an efficient S-scheme heterojunction depends critically on appropriate band alignment, strong interfacial electric fields, and intimate interfacial contact, which can be achieved through rational composition design and controlled assembly strategies.

Herein, we report the construction of a novel $Mn_{0.5}Cd_{0.5}S$/BiOCl (MCS/BiOCl) S-scheme heterojunction for the efficient photocatalytic degradation of CIP. $Mn_{0.5}Cd_{0.5}S$ nanoparticles were synthesised *via* a facile hydrothermal method and subsequently anchored onto BiOCl nanosheets using a green, solvent-free mechanochemical process, which ensures intimate interfacial contact and abundant clean heterojunction interfaces. The resulting composite integrates the broad visible-light absorption of the Mn–CdS alloy with the layered BiOCl scaffold, effectively suppressing charge recombination and enhancing interfacial charge transfer. Comprehensive structural, optical, and electrochemical characterisations confirm the successful formation of the heterojunction and an S-scheme band configuration. The MCS/BiOCl composite exhibits markedly enhanced visible-light-driven photocatalytic degradation of CIP, with good stability and reusability. Radical scavenging experiments identify superoxide and hydroxyl radicals as the dominant reactive species. This work presents a rational design strategy for constructing efficient S-scheme heterojunction photocatalysts for the remediation of pharmaceutical pollutants and provides mechanistic insights into the roles of band alignment and interfacial electric fields in ROS-driven photocatalytic processes.

2 Experimental

2.1 Chemicals

All reagents were purchased from Merck (analytical grade) and used as received without further purification. The following were employed in the syntheses: bismuth(III) nitrate pentahydrate ($Bi(NO_3)_3\cdot5H_2O$, ≥98%), potassium chloride (KCl, ≥99%), manganese(II) acetate tetrahydrate ($Mn(CH_3COO)_2\cdot4H_2O$, ≥99%), cadmium(II) acetate dihydrate ($Cd(CH_3COO)_2\cdot2H_2O$, ≥99%), thiourea (CH_4N_2S, ≥99%), and absolute ethanol (≥99.8%). For photoelectrochemical measurements, sodium sulfate (Na_2SO_4, ≥99%) was used as the electrolyte. Where applicable, slurries were prepared with PVDF/NMP and coated onto a fluorine-doped tin oxide (FTO) substrate.

2.2 Synthesis of $Mn_{0.5}Cd_{0.5}S$ nanoparticles

$Mn_{0.5}Cd_{0.5}S$ nanoparticles were synthesised *via* a one-pot hydrothermal method.[26] In a typical procedure, manganese(II) acetate tetrahydrate ($Mn(CH_3COO)_2\cdot4H_2O$, 1 mmol, 245.1 mg) and zinc(II) acetate dihydrate ($Zn(CH_3COO)_2\cdot2H_2O$, 1 mmol, 219.5 mg) were dissolved in 30 mL of deionised water under magnetic stirring to obtain a homogeneous precursor solution. Thiourea (CH_4N_2S, 4 mmol, 304.5 mg) was then added as the sulfur source, and the mixture was stirred for an additional 30 minutes at room temperature. The resulting clear solution was transferred into a 50 mL Teflon-lined stainless-steel autoclave, sealed, and heated at 180 °C for 12 hours under autogenous pressure. After natural cooling to room temperature, the yellow precipitate was collected by centrifugation (4000 rpm, 10 min), washed thoroughly with deionised water and ethanol to remove residual ions and organics, and dried at 60 °C overnight under ambient conditions.

2.3 Synthesis of BiOCl nanosheets

BiOCl nanosheets were synthesised *via* a hydrothermal method.[27] Bismuth nitrate pentahydrate ($Bi(NO_3)_3\cdot5H_2O$, 1.0 mmol, 485.0 mg) was dissolved in 10 mL of deionised water

under continuous stirring. Separately, potassium chloride (KCl, 1.0 mmol, 74.6 mg) was dissolved in 20 mL of deionised water. The two solutions were then combined under vigorous stirring, forming a uniform suspension. The mixture was stirred for an additional 30 minutes at room temperature to ensure complete mixing. The resulting suspension was transferred to a 50 mL Teflon-lined stainless-steel autoclave, sealed, and heated at 180 °C for 12 hours. After natural cooling to room temperature, the white precipitate was collected by centrifugation, washed thoroughly with deionised water and ethanol to remove residual ions, and dried at 60 °C overnight.

2.4 Synthesis of $Mn_{0.5}Cd_{0.5}S$/BiOCl heterojunction

The $Mn_{0.5}Cd_{0.5}S$/BiOCl heterojunction was fabricated through a solvent-free mechanochemical method. In a typical procedure, BiOCl powder (1.0 g) was mixed with $Mn_{0.5}Cd_{0.5}S$ (MCS, 30 wt% relative to BiOCl, *i.e.*, 0.30 g) and transferred into a zirconia milling jar containing zirconia balls, maintaining a ball-to-powder mass ratio of 10 : 1. The mixture was subjected to high-energy ball milling at 400 rpm for 2 hours using a cyclic milling protocol (10 min on/5 min off) to prevent overheating and preserve crystallinity. After milling, the resulting yellowish composite powder was collected and stored in a desiccator for further characterisation and photocatalytic testing. The as-prepared material is denoted as $Mn_{0.5}Cd_{0.5}S$/BiOCl.

2.5 Photocatalytic degradation of ciprofloxacin experiment

Photocatalytic tests were conducted in a 100 mL Quartz reactor equipped with a magnetic stir bar and an external recirculating water bath to maintain an ambient temperature of 25 ± 2 °C, with illumination provided by a 50 W white LED array positioned ~10 cm from the reactor at a horizontal incidence. In a typical run, 50 mL of a 5 mg L^{-1} CIP solution was added to the reactor with 50 mg of catalyst, and the suspension was stirred at approximately 600 rpm while being purged with air for 10 minutes to ensure adequate dissolved oxygen availability. The initial pH was left unadjusted unless otherwise stated. Prior to illumination, the catalyst-pollutant mixture was equilibrated in the dark for 30 min to establish adsorption–desorption equilibrium, with the concentration at the end of this period taken as C_0 for kinetic calculations. Photocatalysis was then conducted for 90 min under continuous 50 W LED irradiation, during which ~3 mL aliquots were withdrawn every 15 min, immediately filtered through a 0.22 μm PTFE membrane to remove catalyst particles, and analysed by UV-vis spectroscopy. Concentrations were determined from a calibration curve prepared with standard CIP solutions, using absorbance at 277 nm, and the residual concentration was expressed as $C_t/C_0 = A_t/A_0$, assuming a linear relationship between absorbance and concentration. Apparent pseudo-first-order kinetics were calculated using $\ln(C_0/C_t) = k \times t$, where k is the observed rate constant, and t is the irradiation time. Control experiments were performed without light or a catalyst to account for photolysis and adsorption effects. For reusability tests, the spent catalyst was recovered by centrifugation, washed with deionised water and ethanol, dried at 60 °C, and reused under identical conditions, with activity retention expressed as the ratio of k in subsequent cycles to that in the first cycle. A Shimadzu TOC-V analyser was employed to quantitatively evaluate the degree of CIP mineralisation both before and after the photocatalytic reaction.

2.6 Determination of reactive oxygen species

The contribution of different reactive oxygen species (ROS) to CIP degradation was investigated through radical scavenging experiments. *p*-Benzoquinone was employed as a scavenger for superoxide radicals ($\cdot O_2^-$), ethylenediaminetetraacetic acid disodium salt (EDTA-Na) was used to quench photogenerated holes (h^+), and isopropanol (IPA) was applied as a hydroxyl radical ($\cdot OH$) scavenger.[28] In each test, the desired scavenger was added to the photocatalytic reaction mixture at an optimised concentration prior to illumination, while all other experimental conditions were maintained as identical as possible to the standard photocatalytic run. The inhibition effect on CIP degradation was evaluated by comparing the degradation efficiency and apparent rate constants (k) in the presence of each scavenger with those from the control experiment without scavengers, thereby identifying the predominant ROS involved in the photocatalytic process.

3 Results and discussion

3.1 Structure and morphology

The diffraction pattern of the $Mn_{0.5}Cd_{0.5}S$/BiOCl heterojunction shows reflections from both parent lattices without extra peaks from secondary phases, indicating that the heterostructure retains the crystal structures of $Mn_{0.5}Cd_{0.5}S$ and BiOCl without the formation of a new crystalline phase confirming that the composite is formed by physical coupling rather than by a new compound (Fig. 1a). The BiOCl component matches the tetragonal matlockite phase (*P*4/*nmm*), with dominant (001) and (002) basal reflections at low angles (~12° and ~25° 2θ, Cu Kα), and higher-angle peaks assignable to (110)/(101), (102), (112) and (200), consistent with preferential exposure of {001} facets.[29] The sulfide phase is indexed to hexagonal wurtzite CdS-type reflections (100) 24.8°, (002) 26.5°, (101) 28.2°, (102) 36.7°, (110) 43.8°, (103)/(112) 47–52° but with slight peak shifts to higher 2θ compared with pristine CdS, indicative of lattice contraction due to substitution of smaller Mn^{2+} for Cd^{2+} and thus formation of a solid solution rather than a simple physical mixture.[30] Peak broadening of the $Mn_{0.5}Cd_{0.5}S$ reflections relative to BiOCl points to nanoscale crystallites and interfacial microstrain, in line with the SEM observation of nanograins decorating BiOCl nanosheets.[31] The preservation of BiOCl lattice parameters (no systematic shift of its (00l) spacings) suggests negligible Cd/Mn incorporation into BiOCl, while the coexistence of sharp BiOCl peaks and broadened alloy peaks evidences intimate contact between a well-crystallised 2D host and ultra-fine sulphide domains. Collectively, the XRD results verify the phase purity of the heterojunction and support the microstructural picture required for efficient interfacial charge separation.

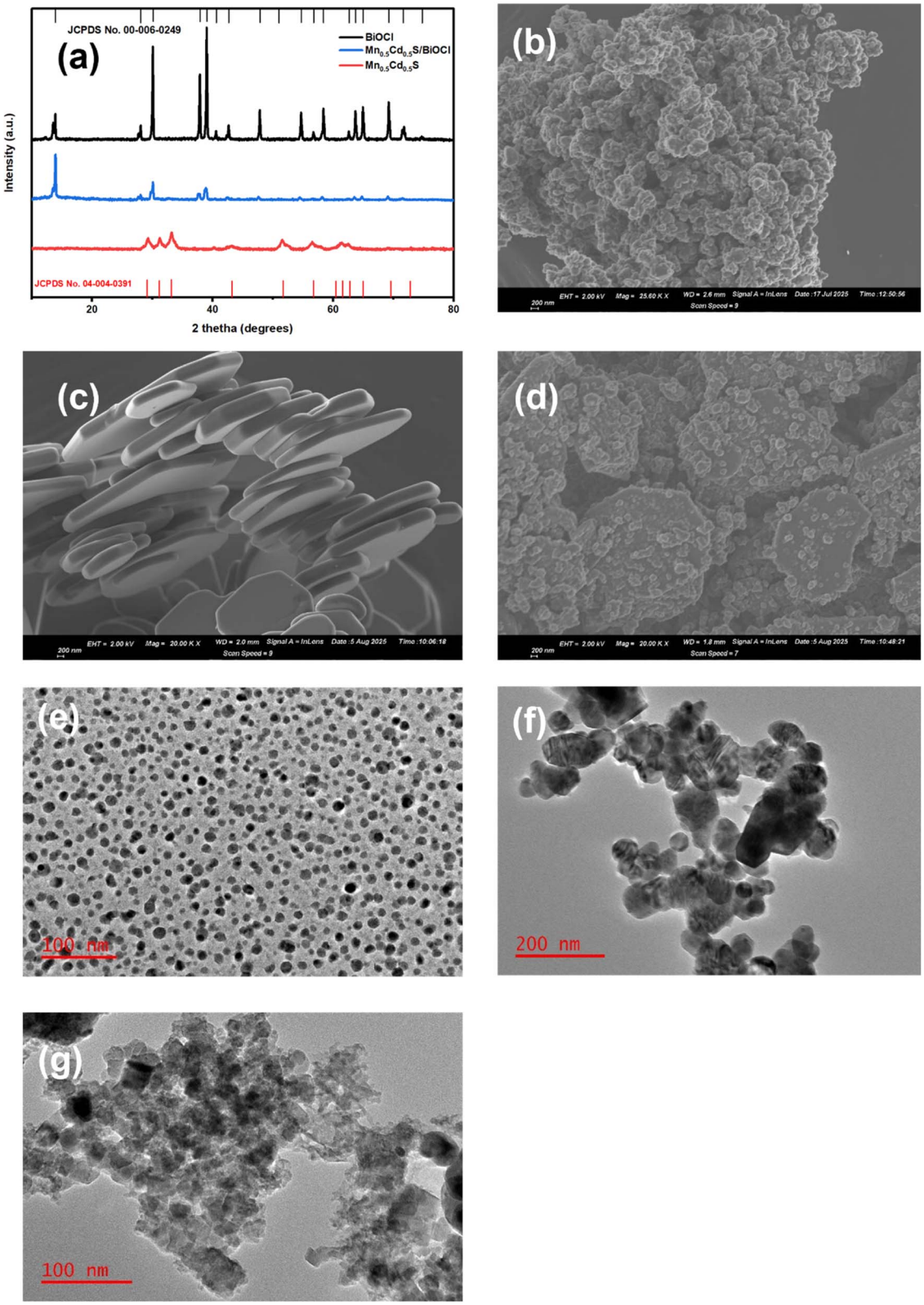

Fig. 1 (a) XRD spectra of MCS, BiOCl and MCS/BiOCl; SEM images of (b) MCS (c) BiOCl (d) MCS/BiOCl; TEM images of (e) MCS (f) BiOCl (g) MCS/BiOCl.

The FE-SEM image confirms that $Mn_{0.5}Cd_{0.5}S$ nanoparticles are intimately anchored on the surfaces and edges of plate-like BiOCl. The BiOCl forms stacked, faceted nanosheets with lateral dimensions of several hundred nanometres (Fig. 1c), while the $Mn_{0.5}Cd_{0.5}S$ appears as nearly isotropic nanograins (tens of nanometres) that decorate the {001} facets and step edges, with

a slightly higher density at ridge/edge sites (Fig. 1b). This conformal decoration produces abundant, clean heterointerfaces and percolating interparticle contacts without obscuring the lamellar BiOCl morphology (Fig. 1d). Such intimate junctions, together with the strong contrast in work function between BiOCl and Mn-doped CdS, are expected to generate a built-in electric field and band bending across the contact, facilitating directional carrier separation (commonly discussed as an S-scheme for BiOCl/CdS couples: electrons retained on Mn–CdS for reduction, holes on BiOCl for oxidation) while providing high densities of active edge/grain-boundary sites. The nanoscale dispersion of $Mn_{0.5}Cd_{0.5}S$ also increases visible-light harvesting relative to pristine BiOCl, whereas the two-dimensional BiOCl scaffold helps suppress hard agglomeration and short diffusion pathways. Overall, the observed architecture is consistent with a robust $Mn_{0.5}Cd_{0.5}S$/BiOCl heterojunction designed to promote interfacial charge separation and accelerate surface redox reactions.

The chemical composition of the synthesised BiOCl, $Mn_{0.5}Cd_{0.5}S$ and $Mn_{0.5}Cd_{0.5}S$/BiOCl was qualified by X-ray photoelectron spectroscopy. The survey XPS spectra for all the materials are displayed in Fig. 2a, which are adjusted by the C 1s peak (284.8 eV). All the elements (Bi, O, Cl, Mn, Cd and S) are detected in the composite $Mn_{0.5}Cd_{0.5}S$/BiOCl, confirming the successful preparation of the material. The characteristic peaks of BiOCl observed in the pure BiOCl and the composite are Bi 4p, Bi 4f, Bi 4d and Cl 2p. In the magnified Bi 4f spectrum shown in Fig. 2b, the two peaks at 164.9 eV and 159.7 eV in the pristine BiOCl are ascribed to Bi $4f_{5/2}$ and Bi $4f_{7/2}$ of Bi^{3+}, respectively.[32] These peaks exhibited a shift to lower binding energy in the MCS/BiOCl composite, indicating electron transfer between BiOCl and MCS. A similar negative shift in binding energies was observed in the Cl 2p peaks found at 199.9 eV and 198.4 eV corresponding to Cl $2p_{1/2}$ and Cl $2p_{5/2}$, respectively,[22] found in the BiOCl only, which shifted to 199.7 eV and 198.2 eV in the composite (Fig. 2c). Additionally, positive shifts in the binding energies of the characteristics of MCS in the composite confirmed an interaction between MCS and BiOCl, resulting in the formation of a heterojunction. For example, in Fig. 2d, the binding energies of Mn 2p found at 652.6 eV and 641.6 eV, corresponding to Mn $2p_{1/2}$ and Mn $2p_{3/2}$, respectively,[23] in the MCS shifted to 652.8 eV and 641.8 eV in the composite. The peaks at 411.9 eV and 405.1 eV assigned to Cd $3d_{3/2}$ and Cd $3d_{5/2}$, respectively,[33–35] also showed a positive shift in the composite (Fig. 2e). The changes in the binding energies of both BiOCl and MCS in the MCS/BiOCl system indicate the flow of electrons from MCS to BiOCl, resulting in the formation of a heterojunction that is practical for photocatalytic reactions.

3.2 N_2 adsorption–desorption

All samples display mesoporous isotherms measured at 77 K, but with clear morphology-dependent signatures (Fig. 3). BiOCl shows a type-IV isotherm with a pronounced H3 hysteresis loop, characteristic of non-rigid aggregates of plate-like particles that generate slit-shaped interlayer pores fully consistent with the stacked-nanosheet SEM.[36] The overall uptake is modest, reflecting the strong restacking of sheets and the correspondingly low specific surface area. $Mn_{0.5}Cd_{0.5}S$ (MCS) presents a type-IV isotherm with a broader H2-like hysteresis, indicative of disordered mesopores formed at the contacts of agglomerated nanograins; its higher uptake corresponds to a larger S_{BET} and pore volume than BiOCl. The MCS/BiOCl heterojunction combines these features: a type-IV isotherm with an H3 loop dominated by the lamellar host but with increased uptake relative to pristine BiOCl, evidencing that MCS nanograins mitigate sheet restacking and introduce additional interparticulate voids. BJH pore-size distributions for all materials are centred in the mesopore regime (~4–20 nm) with negligible microporosity, where BiOCl exhibits mainly slit-like pores between sheets, MCS shows broader intergranular mesopores, and the composite inherits a hierarchical pore system (slit-like + interparticle). This evolution in texture, BiOCl (lowest area) < MCS/BiOCl < MCS (highest area), is favourable for photocatalysis/electrocatalysis, as it increases accessible active sites and facilitates mass transport while preserving the intimate heterointerfaces required for efficient charge separation.

3.3 Optical absorption and band gaps

As shown in Fig. 4a, diffuse-reflectance spectra exhibit a steep edge for BiOCl in the near-UV (approximately 370 nm), consistent with a wide-gap oxide–halide that absorbs weakly in the visible range. By contrast, $Mn_{0.5}Cd_{0.5}S$ (MCS) exhibits strong visible absorption with an edge of approximately 585 nm. The MCS/BiOCl composite inherits the visible response of MCS and exhibits uniformly higher absorbance *ca.* 625 nm, indicating more effective light harvesting together with mild tailing attributable to interfacial/defect states. Tauc plots yield band gaps of 3.27 eV for BiOCl and 1.99 eV for MCS (Fig. 4b); the composite follows the narrower MCS gap, consistent with physical coupling rather than formation of a new bulk phase.

Mott–Schottky plots exhibit positive slopes for both semiconductors, confirming n-type behaviour. Extrapolation gives flat-band potentials of E_{fb}(BiOCl) = −0.21 V and E_{fb}(MCS) = −1.01 V (*vs.* RHE at the measurement pH). For n-type materials, the conduction-band edge is close to the flat band, so we take E_{CB}(BiOCl) = −0.21 V and E_{CB}(MCS) = −1.01 V. Using the optical gaps above, E_{VB}(BiOCl) = E_{CB} + E_g = +3.06 V, and E_{VB}(MCS) = +0.98 V (all *vs.* RHE). This alignment is highly favourable for an S-scheme heterojunction: upon contact, Fermi-level equilibration creates an internal field such that, under illumination, the lower-energy electrons in BiOCl's CB recombine across the interface with the lower-energy holes in MCS's VB.[30] The high-energy electrons are retained on MCS (−1.01 V), sufficiently negative to reduce O_2 to $\cdot O_2^-$, while strongly oxidising holes remain on BiOCl (+3.06 V), positive enough to generate $\cdot$OH from H_2O. Thus, the junction preserves the carriers with the greatest redox power. Fig. 4c shows the band alignment.

Nyquist plots are well described by a Randles circuit (R_s–(R_{ct}||□ C_{dl})) (Fig. 4d). The semicircle diameter, a proxy for charge-transfer resistance, decreases markedly in the order BiOCl ≫ MCS > MCS/BiOCl. From the arc spans, R_{ct} ≈ 1.5–1.6 kΩ (BiOCl), 0.7–0.8 kΩ

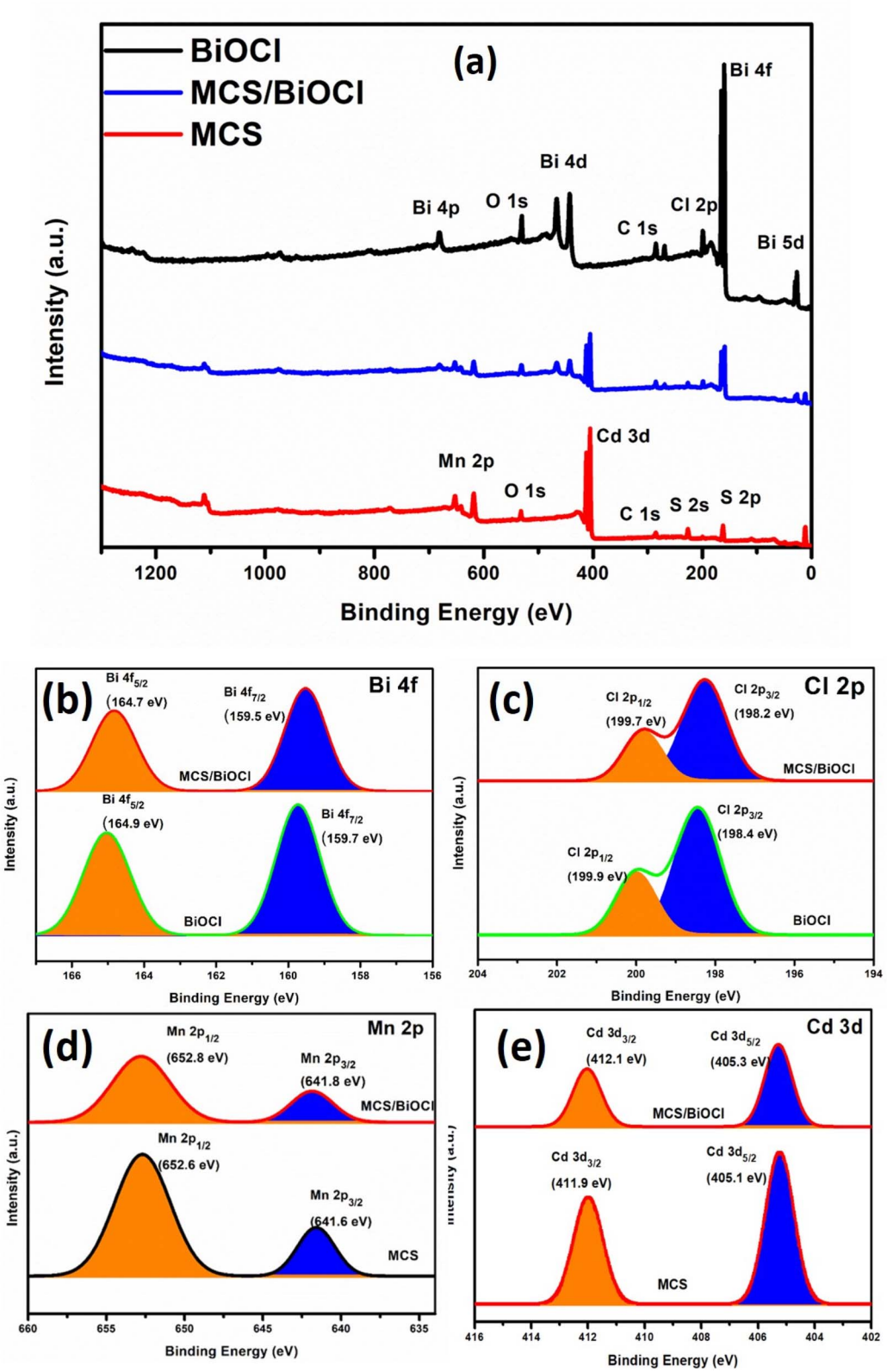

Fig. 2 (a) XPS survey spectra of MCS, BiOCl and MCS/BiOCl. High resolution XPS scan spectra of (b) Bi 4f (c) Cl 2p (d) Mn 2p (e) Cd 3d.

(MCS), and only 60–90 Ω (MCS/BiOCl). This 10 times reduction in the composite evidences much faster interfacial electron transfer, consistent with the built-in field inferred from the Mott–Schottky analysis and the intimate nanosheet–nanograin contacts observed by microscopy. Steady-state photoluminescence is strongest for BiOCl, weaker for MCS, and strongly quenched for MCS/BiOCl,

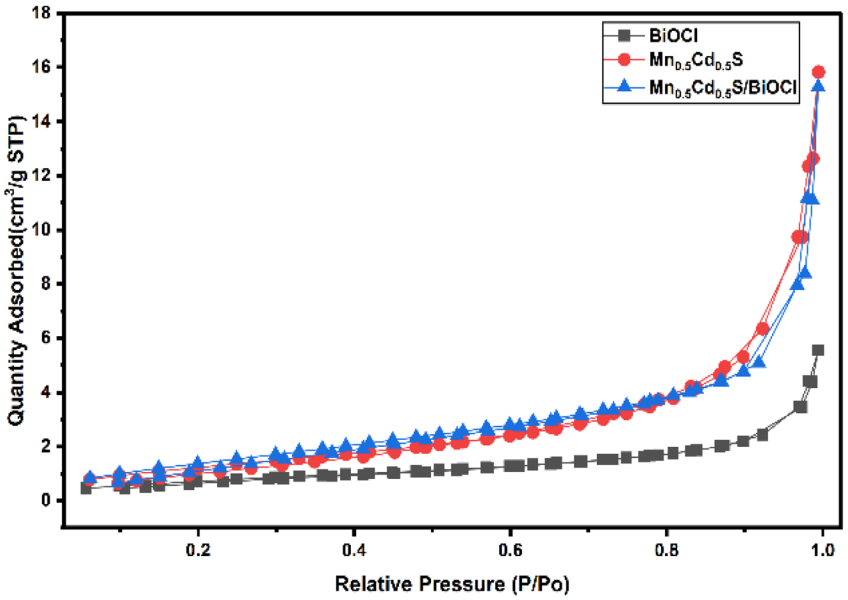

Fig. 3 Nitrogen adsorption–desorption isotherms of BiOCl, MCS and MCS/BiOCl.

indicating suppressed radiative recombination due to efficient interfacial separation. Transient photocurrent measurements (Fig. 4e) under chopped illumination corroborate this: the composite shows the highest and most stable response (typically 0.20–0.24 mA cm^{-2}), exceeding MCS (0.08–0.10 mA cm^{-2}) and BiOCl (0.03–0.05 mA cm^{-2}). The rapid on/off transients and minimal decay further support faster carrier generation/collection with fewer surface traps. The photoluminescence (PL) spectra in Fig. 4f provide insight into the charge recombination behaviour of BiOCl, MCS and the MCS/BiOCl heterojunction. Pristine BiOCl exhibits the highest PL intensity, indicating severe radiative recombination of photogenerated electron–hole pairs, while MCS shows a relatively lower intensity, reflecting moderately improved charge separation. In contrast, the MCS/BiOCl composite displays pronounced PL quenching, evidencing significantly suppressed recombination due to efficient interfacial charge transfer. This behaviour is attributed to the built-in electric field and S-scheme charge-transfer pathway at the MCS/BiOCl interface, where low-

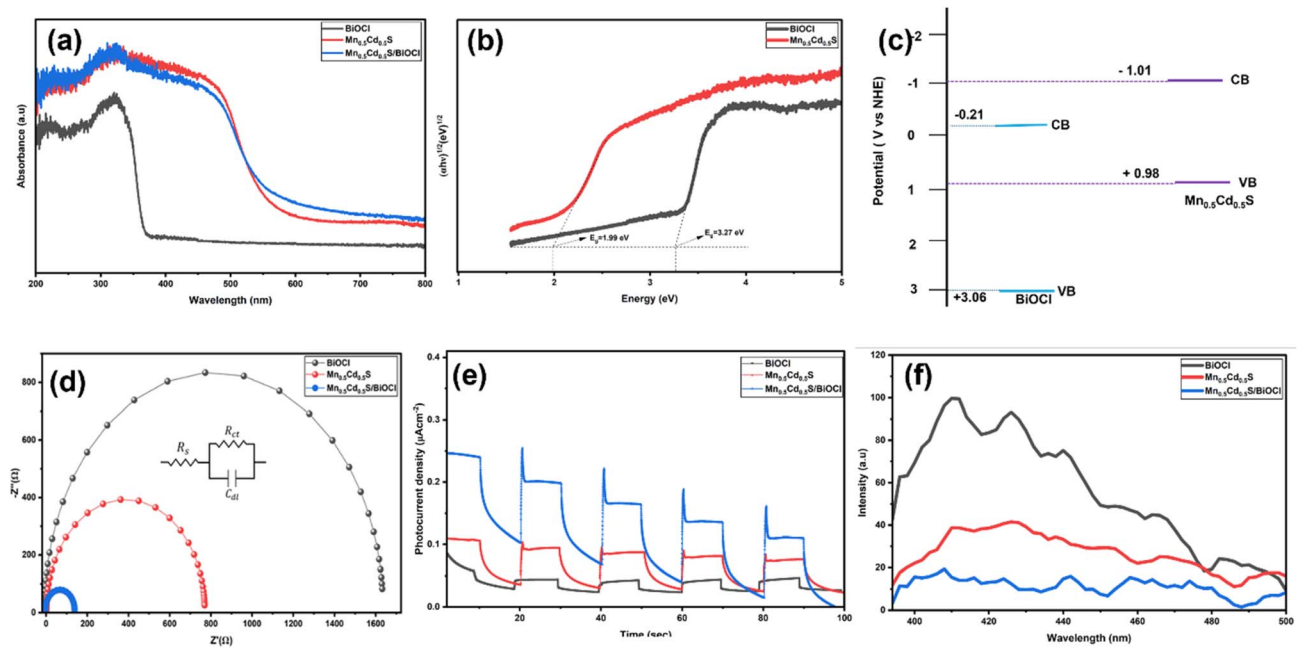

Fig. 4 (a) UV-vis DRS spectra (b) Tauc plot (c) band alignment (d) Nyquist plot (e) photocurrent response (f) photoluminescence spectra of BiOCl, MCS, MSC/BiOCl.

energy charge carriers recombine while high-energy electrons and holes are retained on MCS and BiOCl, respectively. The PL results, therefore, corroborate the electrochemical and photocurrent analyses, confirming enhanced charge separation as a key factor underlying the superior photocatalytic performance of the heterojunction.

Collectively, the optical, electrochemical, and photophysical data converge on a coherent mechanism. MCS broadens visible-light absorption; Mott–Schottky-derived band edges (E_{CB}/E_{VB} = −1.01/+0.98 V for MCS and −0.21/+3.06 V for BiOCl) enable an S-scheme band alignment that preserves highly reducing electrons on MCS and strongly oxidising holes on BiOCl. This interfacial architecture manifests experimentally as dramatically lower R_{ct}, PL quenching, and enhanced photocurrent, all of which explain the superior photo(electro)catalytic behaviour of the $Mn_{0.5}Cd_{0.5}S$/BiOCl heterojunction relative to its individual components.

3.4 Degradation of ciprofloxacin

The photocatalytic activities of BiOCl, MCS and $Mn_{0.5}Cd_{0.5}S$/BiOCl were tested for the amelioration of CIP from wastewater under visible light irradiation. Before exposure to light, the suspension of each photocatalyst in the CIP solution was maintained under dark conditions for 20 min to attain adsorption–desorption equilibrium. As presented in Fig. 5a, the pristine MCS and BiOCl displayed modest degradation efficiency of 67% and 53%, respectively, towards CIP elimination after 120 min. Remarkably, the MCS/BiOCl heterojunction achieved an exceptional 92.3% removal of CIP within the same time frame. The outstanding performance of the composite was attributed to improved light harvesting and enhanced photoactive radical formation, resulting from better charge separation through the formation of a heterojunction. The extent of mineralisation was equally investigated through TOC removal analysis, and the composite material also displayed the highest TOC removal of 61.4% after 120 min (Fig. 5b).

The degradation kinetics were modelled using pseudo-first-order kinetics (Fig. 5c). The heterojunction exhibited superior performance with an apparent reaction rate constant (k) of 0.0221 min^{-1}, which was more than twice that of MCS (0.0087 min^{-1}) and approximately four times the value obtained using pristine BiOCl (0.0059 min^{-1}). This further revealed that the photocatalytic degradation reaction was fastest and most favourable using the composite due to improved separation and migration of charge carriers.

The photocatalytic degradation of CIP is typically influenced by the solution pH. Hence, the degradation experiment with MCS/BiOCl was carried out in different solution pH within the range of 3 to 11. As depicted in Fig. 5d, the photocatalytic degradation of CIP increased from pH 3 to 7 and after which a decline was observed in the basic pH range. This trend can be related to the pH-dependent structure of CIP. At the acidic region (below pH 6.09), CIP molecules are positively charged and negatively charged above pH 8.74.[37] At high acidic and basic pH levels, electrostatic repulsion may occur between the CIP species and the MCS/BiOCl photocatalyst, resulting in lower degradation efficiency. However, since CIP exists as a zwitterionic species within a pH range of 6.09 and 8.74,[26] its degradation is more favourable within this pH range, and hence the best percentage removal was recorded at pH 7. Additionally, superoxide radicals, which also contribute to CIP degradation, can react with excess hydroxide and hydrogen ions across a wide pH range, resulting in lower degradation efficiency.[38] Hence, the degradation of CIP using MCS/BiOCl was performed at neutral pH in this study.

The stability and reusability of the MCS/BiOCl heterostructure composite are crucial for its potential as a photocatalyst in wastewater treatment. Therefore, the material was applied for six consecutive photocatalytic experiments. After each cycle, the photocatalyst was regenerated and reused. As shown in Fig. 5e, after the sixth cycle, the degradation efficiency decreased from 92% to 88.1%, representing an approximate 4% change. This revealed that the photocatalyst is highly reusable, with only a slight loss of photocatalytic efficiency. Additionally, after the sixth cycle, there was no change in the structural and surface morphology of the photocatalyst as seen in the XRD and SEM images of the used material, suggesting good stability with no significant leaching.

In view of real-world applications, the prepared catalysts were tested for their ability to remove CIP from real wastewater. Unlike synthetic laboratory solutions, real water contains a diverse range of natural organic matter (NOM), dissolved inorganic ions and radical scavengers, which can interfere with photocatalytic activity by blocking active sites or deactivating reactive oxygen species. The MCS/BiOCl achieved a degradation efficiency of approximately 83% which was higher than that of MCS (32%) and BiOCl (27%) (Fig. 5c). The observed decrease in degradation efficiency in real water compared to laboratory conditions is primarily due to the interference of scavenger ions, such as carbonates and chloride, which react with hydroxyl and superoxide radicals, thereby limiting their availability for pollutant breakdown. Moreover, competition between NOM and CIP molecules for adsorption sites on the catalyst surface further diminishes degradation efficiency. Despite these challenges, the MCS/BiOCl composite exhibited decent photocatalytic activity, indicating its robustness and suitability for real-world wastewater treatment applications.

Moreover, as shown in Table 1, the MCS/BiOCl exhibits great potential for removing CIP compared to other heterostructure catalysts used for photocatalytic CIP degradation. The percentage removal achieved with the use of MCS/BiOCl was higher than that of some earlier reported heterostructure photocatalysts, suggesting the superiority of the MCS/BiOCl S-scheme heterostructure.

3.4.1 Photodegradation mechanism. To unravel the photodegradation mechanism, it is important to investigate the main radicals generated in the solution that are responsible for the oxidation of CIP molecules. This was achieved by performing the photocatalytic degradation process in the presence of disodium ethylenediamine tetraacetate (EDTA), isopropanol (IPA) and *p*-benzoquinone (*p*-BQ), which acted as masking agents for photogenerated holes, hydroxyl radicals and superoxide radicals, respectively. As depicted in Fig. 6a, a sharp and

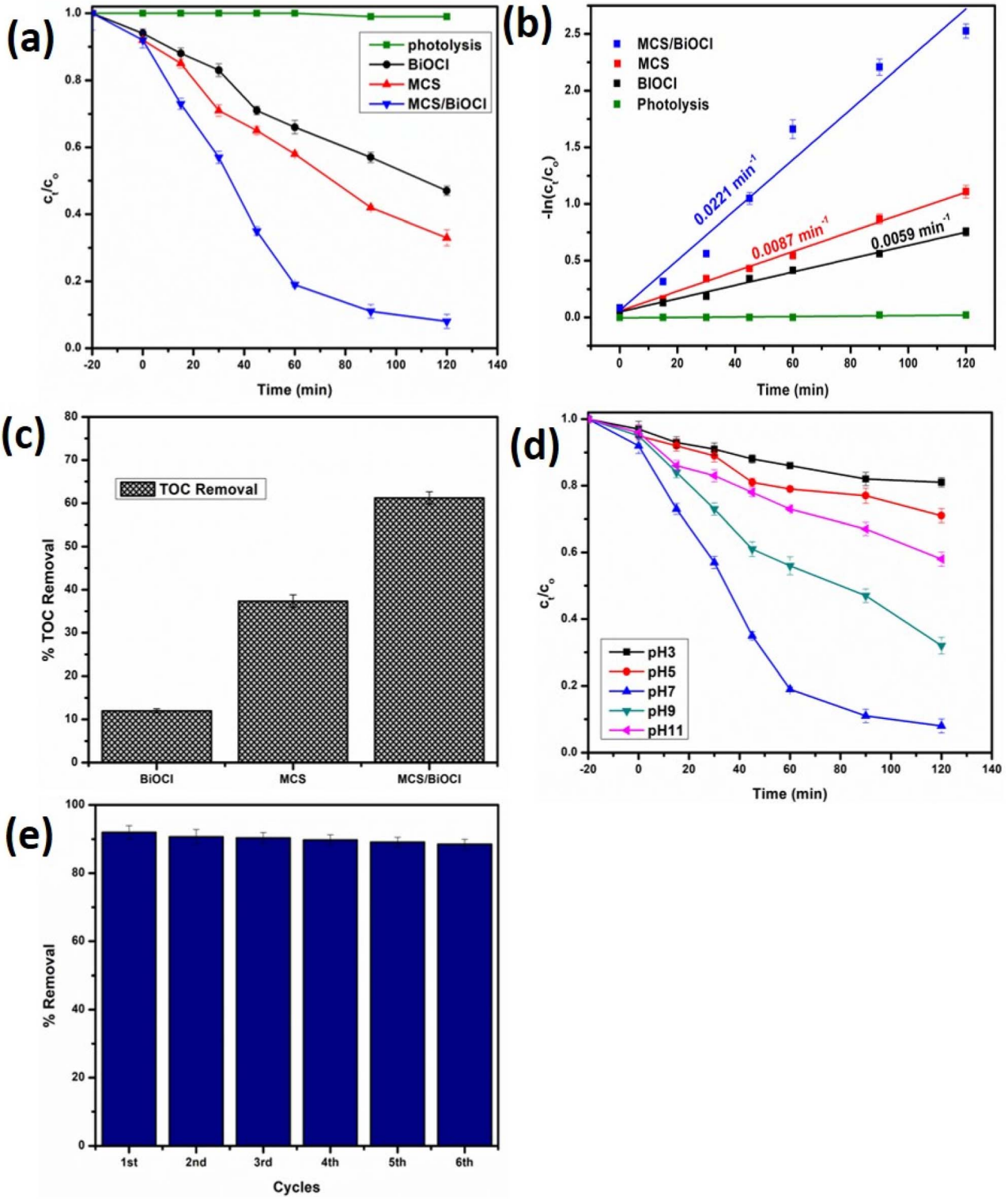

Fig. 5 (a) CIP degradation and (b) fitting of kinetic data using pseudo-first-order kinetics, (c) TOC removal, (d) effect of pH, (e) stability studies.

significant decrease in degradation efficiency, from 92% to 33.7%, was observed upon the addition of IPA, suggesting that photogenerated hydroxyl radical played a major role in the degradation process. Additionally, the degradation efficiency decreased to 45.9% and 68.4% with the addition of pBZQ and EDTA, respectively, suggesting that superoxide radicals and photogenerated holes also contributed to the degradation process.

As proposed in Fig. 6b, the enhanced photocatalytic degradation performance of the $Mn_{0.5}Cd_{0.5}S$/BiOCl core–shell

Table 1 Comparison with other photocatalysts in ciprofloxacin removal

Photocatalyst	Concentration (ppm)	Dose (mg)	Light source	% Removal	Rate constant (min^{-1})	Ref.
Bi-g-C_3N_4	20	50	450 W mercury vapor lamp	79 (60 min)	0.0268	39
$LaFeO_3$/BiOCl	20	20	300 W Xe lamp	88.9 (60 min)	0.01979	40
WO_3/AgI	10	50	1000 W halogen lamp	53.4 (180 min)	0.00415	41
$CaFe_2O_4$/ZnO	10	150	300 W Xe lamp	86.4 (180 min)	—	42
BiOBr/Cu_2S	10	50	1000 W halogen lamp	79.2 (60 min)	0.016	43
BiOBr/TiO_2	20	20	Sunlight	93 (120 min)	0.02262	44
MCS/BiOCl	10	20	300 W Xe lamp	92.3 (120 min)	0.0221	This work

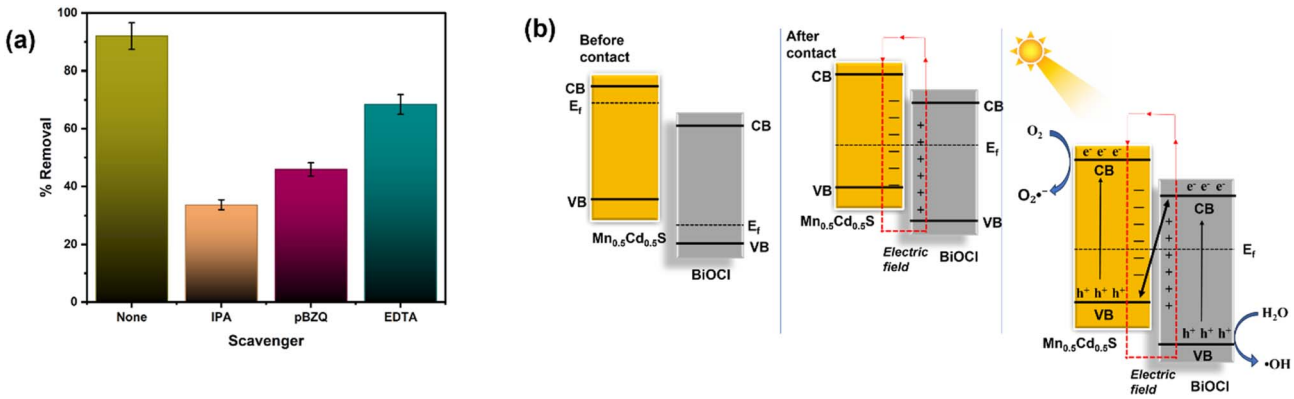

Fig. 6 (a) Radical testing (b) schematic diagram of S-scheme heterojunction formation and photocatalytic mechanism.

heterostructure can be attributed to the formation of an efficient S-scheme heterojunction, which simultaneously promotes charge separation and preserves strong redox capability. Upon light irradiation, both MCS and BiOCl are photoexcited, generating electron–hole pairs within their respective band structures.

$Mn_{0.5}Cd_{0.5}S$, with its narrow band gap, acts as the primary visible-light absorber, producing electrons in its conduction band (CB) and holes in its valence band (VB). BiOCl, although possessing a wider band gap, can also be photoactivated under irradiation due to interfacial effects and defect-assisted absorption. At the MCS/BiOCl interface, an internal electric field is established due to the different Fermi levels and work functions of the two materials. This internal field drives directional charge transfer across the interface.

In the S-scheme configuration, the photogenerated electrons in the CB of BiOCl recombine with the photogenerated holes in the VB of MCS at the interface. This selective recombination pathway effectively eliminates charge carriers with weak redox ability while retaining the highly energetic electrons in the CB of MCS and the strongly oxidative holes in the VB of BiOCl. As a result, the system achieves efficient charge separation without sacrificing redox power, overcoming the limitations of conventional type-II heterojunctions.

The accumulated electrons in the CB of MCS possess sufficient reduction potential to react with dissolved oxygen, generating superoxide radicals ($\cdot O_2^-$). These reactive oxygen species play a crucial role in initiating the degradation of organic pollutants through successive oxidation reactions.[45] Meanwhile, the holes remaining in the VB of BiOCl exhibit strong oxidation ability and can directly oxidise organic molecules or react with surface-adsorbed water or hydroxyl ions to produce hydroxyl radicals ($\cdot OH$), further contributing to pollutant mineralisation.

The synergistic contribution of holes (h^+), superoxide radicals ($\cdot O_2^-$), and hydroxyl radicals ($\cdot OH$) ensures rapid and efficient degradation of the target pollutants. Additionally, the core–shell architecture shortens the charge migration distance and provides intimate interfacial contact, which minimizes bulk recombination and enhances the stability of the heterojunction during photocatalytic reactions.

Overall, the superior photocatalytic activity of the MCS/BiOCl system arises from the combined effects of visible-light harvesting by MCS, strong interfacial electric field-driven charge separation, and the preservation of highly reactive charge carriers through the S-scheme mechanism.

5 Conclusion

In summary, a novel $Mn_{0.5}Cd_{0.5}S$/BiOCl S-scheme heterojunction photocatalyst was successfully constructed through the integration of Mn–CdS alloy nanoparticles with layered BiOCl nanosheets using a green, solvent-free mechanochemical approach. Structural and surface analyses confirmed intimate interfacial coupling between the two components without the formation of secondary phases, while textural characterisation

revealed a mesoporous architecture favourable for mass transport and surface reactions. Optical and electrochemical investigations demonstrated broadened visible-light absorption, efficient suppression of charge recombination, and significantly reduced interfacial charge-transfer resistance. Band-edge analysis based on Mott–Schottky measurements verified the formation of an S-scheme heterojunction, which preserves strongly oxidising holes on BiOCl and highly reducing electrons on $Mn_{0.5}Cd_{0.5}S$. As a result of these synergistic effects, the $Mn_{0.5}Cd_{0.5}S$/BiOCl composite exhibited superior visible-light-driven photocatalytic activity toward CIP degradation, achieving high removal efficiency, accelerated reaction kinetics, and substantial mineralisation compared with the pristine components. Radical trapping experiments confirmed that photogenerated holes, superoxide radicals, and hydroxyl radicals jointly governed the degradation process, in agreement with the proposed S-scheme charge-separation mechanism. The photocatalyst also demonstrated good reusability, structural stability, and appreciable performance in real wastewater matrices, underscoring its practical applicability. Hence, this work provides a rational and scalable strategy for constructing efficient S-scheme heterojunction photocatalysts by combining alloy engineering with layered bismuth oxyhalide scaffolds. The insights gained into interfacial charge transfer, band alignment, and reactive species generation offer valuable guidance for the future design of robust, solar-compatible photocatalysts for the remediation of pharmaceutical contaminants in water.

Conflicts of interest

The authors declare that there are no known conflicts of interest, competing financial interest or personal relationship that could have appeared to influence the wrok reported in this paper.

Data availability

The data that support the findings of this study are available from the corresponding authors upon reasonable request.

Supplementary information (SI) is available. See DOI: https://doi.org/10.1039/d6va00032k.

Acknowledgements

This work is supported by the African Research Universities Alliance (ARUA)/Carnegie Early Career Research Fellowship used at the University of Lagos and the University of Pretoria Research Development Program.

References

1 T. K. Kasonga, M. A. A. Coetzee, I. Kamika, V. M. Ngole-Jeme and M. N. Benteke Momba, Endocrine-disruptive chemicals as contaminants of emerging concern in wastewater and surface water: A review, *J. Environ. Manage.*, 2021, **277**, 111485, DOI: 10.1016/j.jenvman.2020.111485.

2 D. O'Flynn, J. Lawler, A. Yusuf, A. Parle-McDermott, D. Harold, T. Mc Cloughlin, L. Holland, F. Regan and B. White, A review of pharmaceutical occurrence and pathways in the aquatic environment in the context of a changing climate and the COVID-19 pandemic, *Anal. Methods*, 2021, **13**, 575–594, DOI: 10.1039/D0AY02098B.

3 B. O. Orimolade, A. O. Oladipo, A. O. Idris, F. Usisipho, S. Azizi, M. Maaza, S. L. Lebelo and B. B. Mamba, Advancements in electrochemical technologies for the removal of fluoroquinolone antibiotics in wastewater: A review, *Sci. Total Environ.*, 2023, **881**, 163522, DOI: 10.1016/j.scitotenv.2023.163522.

4 S. Snowberger, H. Adejumo, K. He, K. P. Mangalgiri, M. Hopanna, A. D. Soares and L. Blaney, Direct Photolysis of Fluoroquinolone Antibiotics at 253.7 nm: Specific Reaction Kinetics and Formation of Equally Potent Fluoroquinolone Antibiotics, *Environ. Sci. Technol.*, 2016, **50**, 9533–9542, DOI: 10.1021/acs.est.6b01794.

5 R. J. A. Felisardo, E. Brillas, E. Bezerra Cavalcanti and S. Garcia-Segura, Revealing degradation of organic constituents of urine during the electrochemical oxidation of ciprofloxacin via boron-doped diamond anode, *Sep. Purif. Technol.*, 2024, **331**, 125655, DOI: 10.1016/j.seppur.2023.125655.

6 P. Mathur, D. Sanyal, D. L. Callahan, X. A. Conlan and F. M. Pfeffer, Treatment technologies to mitigate the harmful effects of recalcitrant fluoroquinolone antibiotics on the environ- ment and human health, *Environ. Pollut.*, 2021, **291**, 118233, DOI: 10.1016/j.envpol.2021.118233.

7 X. Van Doorslaer, J. Dewulf, H. Van Langenhove and K. Demeestere, Fluoroquinolone antibiotics: An emerging class of environmental micropollutants, *Sci. Total Environ.*, 2014, **500–501**, 250–269, DOI: 10.1016/j.scitotenv.2014.08.075.

8 T. L. Yusuf, B. O. Ojo, T. Mushiana, N. Mabuba, O. A. Arotiba and S. Makgato, Synergistically enhanced photoelectrocatalytic degradation of ciprofloxacin via oxygen vacancies and internal electric field on a $NiSe_2/WO_3$ photoanode, *Catal. Sci. Technol.*, 2024, **14**, 6015–6026, DOI: 10.1039/D4CY00729H.

9 M. Coha, G. Farinelli, A. Tiraferri, M. Minella and D. Vione, Advanced oxidation processes in the removal of organic substances from produced water: Potential, configurations, and research needs, *Chem. Eng. J.*, 2021, **414**, 1–26, DOI: 10.1016/j.cej.2021.128668.

10 S. Cheriyamundath and S. L. Vavilala, Nanotechnology-based wastewater treatment, *Water Environ. J.*, 2021, **35**, 123–132, DOI: 10.1111/wej.12610.

11 K. Xie, S. Xu, K. Xu, W. Hao, J. Wang and Z. Wei, BiOCl Heterojunction photocatalyst: Construction, photocatalytic performance, and applications, *Chemosphere*, 2023, **317**, 137823, DOI: 10.1016/j.chemosphere.2023.137823.

12 T. L. Yusuf, B. O. Orimolade, D. Masekela, K. A. Adegoke, K. D. Modibane and S. S. Makgato, BiOX(X=Cl, Br, I)-based S-scheme heterostructure photocatalysts for environmental remediation and energy conversion, *Mater. Today Sustain.*, 2025, **30**, 101115, DOI: 10.1016/j.mtsust.2025.101115.

13 T. H. Ngo, P. N. M. Le, C. H. Truong, N. D. T. Huynh, T. H. Tran, V. H. Luan, B. T. Dang, M. Rafie Johan, S. Sagadevan and M. V. Le, Development of bismuth-rich bismuth oxyhalides based photocatalyst for degradation of a representative antibiotic under simulated solar light irradiation, *J. Photochem. Photobiol., A*, 2024, **446**, 115157, DOI: 10.1016/j.jphotochem.2023.115157.

14 X. Su, J. Yang, X. Yu, Y. Zhu and Y. Zhang, In situ grown hierarchical 50%BiOCl/BiOI hollow flowerlike microspheres on reduced graphene oxide nanosheets for enhanced visible-light photocatalytic degradation of rhodamine B, *Appl. Surf. Sci.*, 2018, **433**, 502–512, DOI: 10.1016/j.apsusc.2017.09.258.

15 Y. Ren, Y. Li, G. Pan, N. Wang, Y. Xing and Z. Zhang, Recent progress in CdS-based S-scheme photocatalysts, *J. Mater. Sci. Technol.*, 2024, **171**, 162–184, DOI: 10.1016/j.jmst.2023.06.052.

16 W. Duan, W. Li, T. Ma, Y. Su and N. Wang, Latest advances in the design, preparation and application of CdS-based photocatalysts, *Chem. Commun.*, 2026, **62**, 4386–4412, DOI: 10.1039/D5CC06668A.

17 T. L. Yusuf, O. C. Olatunde, D. Masekela, N. Mabuba, D. C. Onwudiwe and S. Makgato, Rational design of S-scheme $Cd_{0.5}Zn_{0.5}S/CeO_2$ heterojunction for enhanced photooxidation of antibiotics and photoreduction of Cr(VI), *Ceram. Int.*, 2024, **50**, 45581–45591, DOI: 10.1016/j.ceramint.2024.08.397.

18 S. Keerthana, R. Yuvakkumar, G. Ravi, A. E.-Z. M. A. Mustafa, A. A. Al-Ghamdi, M. Soliman Elshikh and D. Velauthapillai, PVP influence on Mn–CdS for efficient photocatalytic activity, *Chemosphere*, 2021, **277**, 130346, DOI: 10.1016/j.chemosphere.2021.130346.

19 M. Xiong, Y. Qin, B. Chai, J. Yan, G. Fan, F. Xu, C. Wang and G. Song, Unveiling the role of Mn-Cd-S solid solution and MnS in MnxCd1-xS photocatalysts and decorating with CoP nanoplates for enhanced photocatalytic H2 evolution, *Chem. Eng. J.*, 2022, **428**, 131069, DOI: 10.1016/j.cej.2021.131069.

20 L. Wang, B. Zhu, J. Zhang, J. B. Ghasemi, M. Mousavi and J. Yu, S-scheme heterojunction photocatalysts for CO_2 reduction, *Matter*, 2022, **5**, 4187–4211, DOI: 10.1016/j.matt.2022.09.009.

21 S. Lei, R. Luo, H. Li, J. Chen, J. Zhong and J. Li, Ionic liquid assisted in-situ construction of S-scheme $BiOI/Bi_2WO_6$ heterojunctions with improved sunlight-driven photocatalytic performance, *Inorg. Chem. Commun.*, 2020, **121**, 108192, DOI: 10.1016/j.inoche.2020.108192.

22 T. L. Yusuf, O. C. Olatunde, D. Masekela, O. D. Saliu, K. D. Modibane and D. C. Onwudiwe, Interfacial S-scheme charge transfer in $MgIn_2S_4/ZnO$ heterojunction for enhanced photodegradation of tetracycline and efficient water splitting, *Nanoscale Adv.*, 2025, **7**, 4876–4885, DOI: 10.1039/D5NA00573F.

23 S. Li, R. Li, K. Dong, Y. Liu, X. Yu, W. Li, T. Liu, Z. Zhao, M. Zhang, B. Zhang and X. Chen, Self-floating $Bi_4O_5Br_2$/P-doped C_3N_4/carbon fiber cloth with S-scheme heterostructure for boosted photocatalytic removal of emerging organic contaminants, *Chin. J. Catal.*, 2025, **76**, 37–49, DOI: 10.1016/S1872-2067(25)64780-2.

24 P. Hao, Y. Cao, X. Ning, R. Chen, J. Xie, J. Hu, Z. Lu and A. Hao, Rational design of CdS/BiOCl S-scheme heterojunction for effective boosting piezocatalytic H_2 evolution and pollutants degradation performances, *J. Colloid Interface Sci.*, 2023, **639**, 343–354, DOI: 10.1016/j.jcis.2023.02.075.

25 S.-S. Wang, X. Liang, Y.-K. Lv, Y.-Y. Li, R.-H. Zhou, H.-C. Yao and Z.-J. Li, Electric Field Coupling in the S-Scheme CdS/BiOCl Heterojunction for Boosted Charge Transport toward Photocatalytic CO_2 Reduction, *ACS Appl. Energy Mater.*, 2022, **5**, 1149–1158, DOI: 10.1021/acsaem.1c03531.

26 Y. Ai, S. A. C. Carabineiro, X. Xiong, H. Zhu, Q. Wang, B. Weng and M.-Q. Yang, Systematic assessment of emerging contaminants elimination using an S-scheme $Mn_{0.5}Cd_{0.5}S/In_2S_3$ photocatalyst: Degradation pathways, toxicity evaluation and mechanistic analysis, *Chin. J. Catal.*, 2025, **75**, 147–163, DOI: 10.1016/S1872-2067(25)64723-1.

27 Y. Huang, F. Chen, Z. Guan, Y. Luo, L. Zhou, Y. Lu, B. Tian and J. Zhang, S-Scheme $BiOCl/MoSe_2$ Heterostructure with Enhanced Photocatalytic Activity for Dyes and Antibiotics Degradation under Sunlight Irradiation, *Sensors*, 2022, **22**, 1–14, DOI: 10.3390/s22093344.

28 D. C. Akintayo, T. L. Yusuf and N. Mabuba, Construction of hierarchical S-scheme $MgIn_2S_4/CeO_2$ heterojunction for boosted photocatalytic oxidation of tetracycline and reduction of Cr(VI), *Colloids Surf., A*, 2025, **721**, 137215, DOI: 10.1016/j.colsurfa.2025.137215.

29 K. Xu, J. Shen, S. Zhang, D. Xu and X. Chen, Efficient interfacial charge transfer of BiOCl-In_2O_3 step-scheme heterojunction for boosted photocatalytic degradation of ciprofloxacin, *J. Mater. Sci. Technol.*, 2022, **121**, 236–244, DOI: 10.1016/j.jmst.2021.12.070.

30 S. Li, C. You, K. Rong, C. Zhuang, X. Chen and B. Zhang, Chemically bonded $Mn_{0.5}Cd_{0.5}S$/BiOBr S-scheme photocatalyst with rich oxygen vacancies for improved photocatalytic decontamination performance, *Adv. Powder Mater.*, 2024, **3**, 100183, DOI: 10.1016/j.apmate.2024.100183.

31 L. Shi, J. Yin, Y. Liu, H. Liu, H. Zhang and H. Tang, Embedding Cu_3P quantum dots onto BiOCl nanosheets as a 0D/2D S-scheme heterojunction for photocatalytic antibiotic degradation, *Chemosphere*, 2022, **309**, 136607, DOI: 10.1016/j.chemosphere.2022.136607.

32 Z. Chen, Y. Ma, W. Chen, Y. Tang, L. Li and J. Wang, Enhanced photocatalytic degradation of ciprofloxacin by heterostructured $BiOCl/Ti_3C_2Tx$ MXene nanocomposites, *J. Alloys Compd.*, 2023, **950**, 169797, DOI: 10.1016/j.jallcom.2023.169797.

33 Y. Liu, L. Wang, H. Lv, X. Wu, X. Xing and S. Song, Constructing robust MoO_2/Au/$Mn_{0.5}Cd_{0.5}S$ multiple heterojunctions for improved photocatalytic hydrogen evolution: An insight into the synergetic effect of MoO2 and Au cocatalysts, *Appl. Surf. Sci.*, 2021, **541**, 148582, DOI: 10.1016/j.apsusc.2020.148582.

34 L. Wang, T. Ma, H. Li, Y. Zhang, Y. Wang, Z. Li and S. Xu, $Mn_{0.5}Cd_{0.5}S$@NiO composite for boosting visible-light-driven photocatalytic hydrogen evolution, *Inorg. Chem. Commun.*, 2024, **160**, 112000, DOI: 10.1016/j.inoche.2023.112000.

35 Y. Wang, W. Li, W. Duan, R. Cui, G. Liao and N. Wang, Hydrophilicity improvement of PVDF-networked CdS/TiO_2 photocatalytic membrane for flat-panel purification of pharmaceutical wastewater accompanied by Cr(VI) reduction, *Chem. Eng. J.*, 2025, **519**, 165220, DOI: 10.1016/j.cej.2025.165220.

36 F. Yuan, Y. Zheng, D. Gao, D. Meng, L. Wang and X. Hu, Relationship of structure and enhanced photocatalytic activity of S-scheme BiOCl/g-C_3N_4 heterojunction for xanthate removal under visible light, *Adv. Powder Technol.*, 2023, **34**, 104049, DOI: 10.1016/j.apt.2023.104049.

37 Y. Fan, J. Xiong, Y. Cai, S. Huang, Y. Liang, S. Jiang and G. Chen, Bi_2MoO_6/g-C_3N_4 S-type heterojunction with oxygen vacancies for enhanced removal of ciprofloxacin: Investigation of degradation efficiency and mechanism, *J. Water Process Eng.*, 2025, **71**, 107157, DOI: 10.1016/j.jwpe.2025.107157.

38 X. Hu, X. Hu, Q. Peng, L. Zhou, X. Tan, L. Jiang, C. Tang, H. Wang, S. Liu, Y. Wang and Z. Ning, Mechanisms underlying the photocatalytic degradation pathway of ciprofloxacin with heterogeneous TiO_2, *Chem. Eng. J.*, 2020, **380**, 122366, DOI: 10.1016/j.cej.2019.122366.

39 P. Saini, K. Ahmadizamani, N. Chakinala, S. Mukherjee, G. Sethia, A. Gupta Chakinala and P. K. Surolia, Bismuth doped g-C_3N_4 composites for enhanced photocatalytic degradation of ciprofloxacin, *J. Mol. Struct.*, 2025, **1321**, 140013, DOI: 10.1016/j.molstruc.2024.140013.

40 J. Wang, Z. Yu, T. Zhao, Y. Song, H. Liu, J. Hou and P. Yu, A core-shell structure formed by A-site defects in $LaFeO_3$/two-dimensional BiOCl nanosheets for highly efficient photocatalytic degradation of ciprofloxacin: Insights into performance and mechanism, *J. Photochem. Photobiol., A*, 2026, **473**, 116908, DOI: 10.1016/j.jphotochem.2025.116908.

41 J. Liu, M. Zhu, W. Yuan, G. Yang, C. Zhang, H. Zhang, D. Zhang, P. Cai and X. Pu, Lamellar WO_3/AgI S-scheme heterojunction for superior visible light driven photocatalytic degradation of ciprofloxacin, *Chem. Eng. Sci.*, 2024, **285**, 119639, DOI: 10.1016/j.ces.2023.119639.

42 H. Ye, J. Du, X. Ding, M. Wang, Z. Zhang and Q. Zhang, $CaFe_2O_4$/Ag/ZnO z-scheme heterojunction material for photocatalytic decomposition of ciprofloxacin, *Chem. Phys. Lett.*, 2024, **842**, 141227, DOI: 10.1016/j.cplett.2024.141227.

43 Z. Kong, R. Zhang, J. Dong, J. Yu, D. Zhang, J. Liu, P. Cai and X. Pu, BiOBr/Cu_2S p–n heterojunction for efficient photodegradation of ciprofloxacin and tetracycline under visible light, *J. Alloys Compd.*, 2024, **990**, 174463, DOI: 10.1016/j.jallcom.2024.174463.

44 M. Shkir and A. M. Ali, Novel 2D/3D BiOBr/TiO_2 S-scheme heterostructures photocatalyst fabrication for remarkable ciprofloxacin degradation under solar light, *FlatChem*, 2025, **52**, 100891, DOI: 10.1016/j.flatc.2025.100891.

45 T. L. Yusuf, S. A. Ogundare, F. Opoku and N. Mabuba, Photoelectrocatalytic degradation of sulfamethoxazole over S–Scheme Co_3Se_4/$BiVO_4$ heterojunction photoanode: An experimental and density functional theory investigations, *Surf. Interfaces*, 2023, **36**, 102534, DOI: 10.1016/j.surfin.2022.102534.